**ROYAL
AERONAUTICAL
SOCIETY**

REGULAR PAPER

An investigation of aerodynamic behaviours and aerodynamic performance of a model wing formed from different profiles

A. Aşkan ⓘ, S. Tangöz* ⓘ and M. Konar ⓘ

Faculty of Aeronautics and Astronautics, Erciyes University, Kayseri, Turkey
*Correspondence author. Email: stangoz@erciyes.edu.tr

Abstract

In this study, the aerodynamic performances and the flow separation behaviour of the wing profiles, used in the wing of Boeing 737-Classic aircraft, and a model wing formed of these profiles were investigated at 2×10^5 Reynolds number (Re) and different angles of attack ranging from $-4°$ to the angle, which maximum lift point obtained. The experiments were conducted in a low-speed wind tunnel in Erciyes University Faculty of Aeronautics and Astronautics Aerodynamic Laboratory. Four profiles and the model wing, which was obtained from the combination of the four profiles were produced in a rectangular shape with dimensions of $0.21\text{m} \times 0.21\text{m}$. In the first part of this two-part study, the wing profiles were examined individually regarding aerodynamic performance and flow separation. In the second phase of the study, the aerodynamic performance and the flow separation behaviour of the model wing were examined and the results were compared with the data obtained from each profile. The study results showed that the slopes of the numerical graphics are generally quite consistent with experimental results. In addition, the pressure and velocity distributions have followed the normal trend until the angle-of-attack (AoA) of $20°$. In contrast, the negative speed values and negative pressure zones have appeared on the profile above this angle. The air flowed as laminar on the profiles and the model wing until $20°$, while laminar separation bubbles are begun to take place at about $24°$ AoA. Finally, the best aerodynamic performance has been obtained with the model wing.

Nomenclature

AoA	angle-of-attack
AR	aspect ratio
C_D	drag coefficient
C_L	lift coefficient
C_{Lmax}	maximum lift coefficient
C_L/C_D	lift coefficient to drag coefficient ratio
C_P	pressure coefficient
D	Drag
Eq.	equation
L	lift
L/D	lift to drag ratio
L/D_{max}	maximum lift to drag ratio
Re	Reynolds number
x/c	location along the cord (mm/mm)
z/b	location along the span (%)

1.0 Introduction

Significant parts of the accidents that occur in the aviation field are triggered by different factors like stall, which are expressed as the inability of the aircraft to hold in the air during takeoff and landing. The reason for the occurrence of the stall event is that the airflow on the wing surface is undesirably separated and the carrying force holding the aircraft in the air drops below the limits of the balance weight of the aircraft. The separation on the wing surface, which is the cause of the stall event, in general, occurs at low speeds and high angles of attack. At low speed, usually, the airflow on the wing in the number zone between 4.0×10^4 and 1.0×10^5 is referred to as the critical Reynolds number interval because of the transition from laminar to turbulent flow [1]. In the critical Reynolds number range, adverse pressure gradients occur and cause the air to break off from the surface. With increasing angle-of-attack, the adverse pressure gradients on the wing surface become more severe, so separation bubbles may form and burst of these bubbles may occur [2]. Due to low Reynolds numbers aerodynamics, the inclination of flow separation on the lifting surfaces creates the most important difficulty. Because of bursting bubbles, "the stall" – the event that aircraft cannot hold in the air – may occur. The variables related to the wing stall are numerous and include the wing profile, wing planform, twist of the wing, surface roughness, flow turbulence and Reynolds number [3]. In particular, at high angles of attack, on the leading edge of medium-thickness profiles, a sudden increase of drag force, a decrease of lifting force and changing of pitching moment has been associated with the sudden bursting of the laminar separation bubble [4]. Lots of work has been done up to this day about the laminar separation bubble and stall event and it is basically aimed to decrease the stall speed [5, 6]. Reducing the stall speed will allow the aircraft to be held in the air and safely fly at low Reynolds numbers.

When aircraft accidents that occurred in recent years are examined, it is seen that the stall from the resulting airflow separation due to power loss, icing and similar causes is considered one of the main reasons for the accidents.

The flow separation, which is the main cause of the stall phenomenon, is caused by the loss of the kinetic energy of the airflow travelling from the leading to the trailing edge on the wing surface and the local positive pressure gradients. At this time, the reverse flow from the trailing edge of the wing triggers separation [7, 8].

If the stall event spreads to the tip of the wing, it will cause a big vibration on the wing, so the aircraft cannot be able to hold in the air. Various techniques such as active and passive flow control methods have been developed to control the flow separation. In this study, unlike these methods, it was aimed to make an improvement in the performance of the wing by combining the different profiles. In particular, thin profiles were used towards the tip of the wing to delay the separation and allow the stall event to arrive the latest on the wing tip.

The investigation and prevention of airflow separation from the wing surface are very crucial topics in literature. In one of these studies [9], the airflow separation is experimentally investigated at low Reynolds numbers. In this study, the NASA low-speed GA (W)-1 profile with 101mm chord length and 17% maximum thickness was investigated at a 0.68×10^5 fixed Reynolds number. When the angle-of-attack was increased from $9°$ to $11°$, it was observed that due to the inverse pressure gradients, at the laminar boundary layer the flow was separated from the upper surface and a bubble formed with 20% of the length of the chord and 1% of the height of the chord length. When the angle-of-attack reached $12°$, it was seen that the bubbles suddenly exploded and stall incident took place. Zanin and colleagues [10] conducted an investigation into the control of flow separation from the wing surface at low Reynolds numbers. In this empirical study, the variations of three-dimensional flow models have been analysed as a function of the shape and position of flow disturbance. The stream was found to have inhibited the formation of large-scale vortices in the separation zone, which can be controlled by mounting in the return flow zone of the separation line towards the flow direction. It was seen the close connection between the vortices and the separation zone and also, it was found to blocking the formation of the vortex structure can result in significant differences in the structure of the dissociation zone. Mack et al. [11] have investigated the flow separation and separation control on NACA 64-618 profile
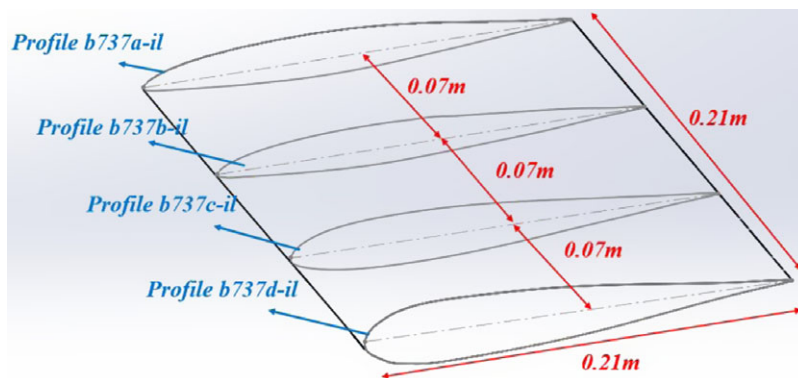
Figure 1. *The placement and distance between profiles on the model wing.*

at two low Reynolds numbers (Re $=137,000$ and Re $= 64,200$) between $-12°$ and $20°$ angle-of-attack. As a result of the experiments carried out, it was seen that the drag forces decreased at Re $= 64,200$, $\alpha = 10°$ and Re $= 137,000$, $\alpha = 6°$. The main cause of this performance increase was understood as sudden reattachment of the flow separated from the profile. Also, in this study, passive and active flow control strategies were investigated to increase the wing performance.

In another study [12] on a wing profile at low Reynolds numbers, the formation of laminar separation bubbles and the motion of bubbles have been investigated. Experiments were carried out on NACA 2,415 wing profile with Re $= 0.5 \times 10^5$ and different angles of attack. As the angle-of-attack increases, a shift towards the edge of the breakpoint is seen. When the angle-of-attack is increased to a certain critical value ($\alpha = 13°$), it is seen that the wing does not seem to be able to hold again. It has been observed that after $12°$ angle-of-attack, there is a serious drop in lift coefficient (C_L).

When the previous studies are examined, it is seen that the flow separation analyses usually focus on profiles or the wings obtained from a certain profile. In this study, aerodynamic performance and flow separation behaviours have been investigated on a model wing made up of different profiles and on different profiles, and a significant contribution has been made to the literature.

2.0 Experimental setup

2.1. Test model and facility

The aerofoils and model wing combination of aerofoils used for present study have rectangular planforms and flat side edges. The wings have been drawn in the Solidworks® program and transferred to the 3D printer. The cord length of the wings is $c = 0.21$m and the aspect ratio is AR $= 1.0$. The model wing is composed of four different profiles. The placement of the profiles and the distance between them on the wing are shown in Fig. 1. Profiles were combined using solid machining with the "loft" command in Solidworks® to obtain a model blade. A smooth and organic geometry is created by transitioning between multiple profiles and guiding them with curves. The wings were made of grey polylactic acid thermoplastic polyester (PLA), and the rough surfaces were smoothed with very precise (2,500 grit) sandpaper.

The aerodynamic coefficients of the wings were measured in a low-speed wind tunnel in the Aerodynamics Research Laboratory at Erciyes University Faculty of Aeronautics and Astronautics (EU-FAA). A schematic of the tunnel is shown in Fig. 2. The wind tunnel is an open-circuit suction type and consists mainly of seven parts [13]. These are the flowing canal, flow regulator sieve flanges, shrinkage cone, test area, diffuser, engine and silencer. The flow is straightened by two metal sieve flanges and passes through multiple settling screens in the bell mouth. Then the flow gets through contracted a 6:1 area ratio and arrived in a test section which has square 0.57 by 0.57m inlet and 0.59 by 0.59m outlet

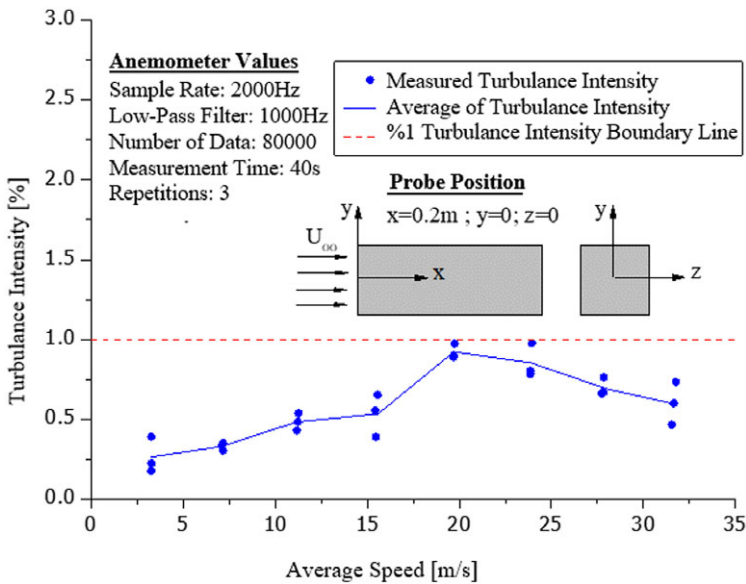**Figure 2.** *Wind tunnel and detailed view of the test section.*

Figure 3. *Turbulence intensity of wind turbine [14].*

and of 1.8m length. The test section is closed type. The operating speed range of the wind tunnel is 3 to 33 m/s (fan speed 150–1,200 rpm) and has high accuracy hotwire and an automatic calibration unit. The flow turbulence intensity shown in Fig. 3 is lower than 0.1% at the range of operating speed [14].

2.2. Test procedure

An anemometer with a pitot tube connected was used to find the air velocity inside the wind tunnel based on the cord length of the wing, which corresponds to a speed of 2.0×10^5 Reynolds number. The lift (L) and drag (D) forces have been measured by a 3-axis force and torque meter (Load cell).

Table 1. *Error measurements lift and drag coefficients of profiles and model wing*

	737a-il	737b-il	737c-il	737d-il	Model Wing
Total error of U_{C_L}	0.0553	0.0548	0.0522	0.537	0.0543
Total error of U_{C_D}	0.1023	0.09273	0.0675	0.0714	0.080

In the experiments, the Ati f/t gamma SI 32-2.5 force/torque sensor was used to measure the forces on the wing and the Drehachse ZD30 traverse device was used as the rotation unit. The load cell has a maximum measurement limit of $\pm 100N$ on the z-axis (F_z) and $\pm 32N$ on the x-axis (F_x) and y-axis (F_y). In addition, the maximum torque (T_x, T_y, T_z) measurement values in three directions are $\pm 2.5Nm$. Although the measurement resolutions vary according to the components, the data acquisition system is 16 bits. The Load cell is calibrated at regular intervals. Different weights between 10g and $-1,000g$ are hung on the load cell one by one, and the calibration process is carried out separately on the x- and y-axis. The models were supported by a strut to the load cell. The strut is attached to 1/4 of the wing cord (aerodynamic center of the wing) from the leading edge along the centre line of the wing. The experiments were carried out at the angle-of-attack ranging from $-4°$ to the highest lift point. The angle sweep started at $-4°$ and the angle increased by $30°$ with $4°$ increments. After $30°$ (if the highest lift point exceeds $30°$), the increases were $2°$. To fully detect maximum lift and maximum lift/drag points the angle was moved $1°$ increment when necessary. After completing the sweep of increased angle-of-attack, each model was returned to the initial angle at the same angle intervals. At each angle change, it was waited 30 seconds for the wing flicker to disappear.

The forces on the load cell were reset and the tunnel was run before recording for 1 min until the stream of air in the tunnel recovered. Recording of force values was continued for 3 min. With the loads from the load cell, the A/D Board records ten values at each second. Averages of the values recorded for 3 min were taken for every angle-of-attack. Each test was performed three times to increase the reliability of the experiments and the average of the three tests obtained was taken and compared with the numerical results. The factors such as the calibration of the devices used in the experiments and environmental conditions may cause an error margin in the analysis results. To determine this margin of error, the uncertainty analysis given by Ref. [15] was applied. Free flow rate, forces, density, temperature etc. Quantities were measured experimentally. With the help of these experimental results, the percentage error of the lift and drag force coefficients was obtained. Equations (1) and (2) have been used to obtain uncertainty analysis.

$$r = kX_1^a X_2^b X_3^c \dots X_n^j \tag{1}$$

The coefficients and exponential expressions of the parameters that affect the "r" value are constant values. The "k" is a constant, and X_n^j is the measured value of an independent variable raised to power.

$$U_r = \frac{W_r}{r} = \sqrt{a^2 \left(U_{X_1}\right)^2 + b^2 \left(U_{X_2}\right)^2 + \dots + c^2 \left(U_{X_n}\right)^2} \tag{2}$$

Here U_{x_n} denotes the uncertainty of the measured independent variable X_n.

Since the uncertainty analysis of dimensionless coefficients such as C_L and C_D varies depending on the environmental conditions and the error margin of the devices, as well as the frontal area of the wings and therefore the thickness of the wings, the uncertainty analysis was calculated for each wing separately. The obtained values are given in Table 1.

3.0 Computational setup and validations

To predict the approach aerodynamic performance, the wing profiles were examined numerically prior to the wind tunnel experiments. ANSYS Fluent Simulation version 16.1 for simulation was used with the "coupled" algorithm and the second-order upwind scheme to solve the steady-state Reynolds-averaged Navier-Stokes equation. The SST k-ω was chosen as the turbulence model to accurately predict the

Table 2. *The characteristics of the profiles*

Profile	Thickness (t/c), %	Camber (f/c), %	Position on Model Wing (% of span)
b737a-il (Profile A)	15.4 % at 19.6 % c	0.2 % at 5.0 % c	0
b737b-il (Profile B)	12.5 % at 29.7 % c	0.8 % at 10.0 % c	33.3
b737c-il (Profile C)	10.0 % at 39.9 % c	1.5 % at 20.4 % c	66.6
b737d-il (Profile D)	10.8 % at 40.0 % c	1.6 % at 20.0 % c	100
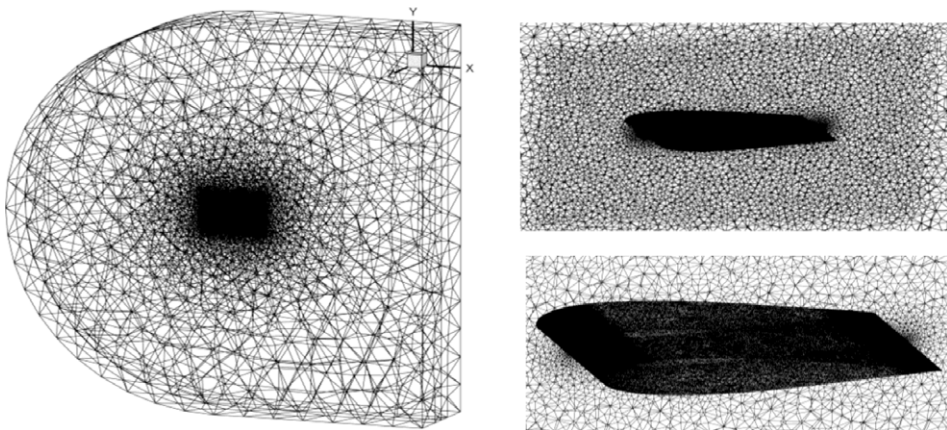
Figure 4. *The geometry and detailed mesh view for analysis.*

inverse pressure gradient flows near the surface of the model and near the transition flow [16, 17, 18]. Each calculation consists of 1,000 iterations. After about 400 iterations, the convergence was caught with a residue of 10^{-4}.

3.1. Simulation details

In this study, the aerodynamic performance of four profiles and a wing, which consisted of those four different profiles were investigated. The wing planforms are square and have a cord length of $c = 0.21$ m. The other specific features of the wing profile are shown in Table 2. To verify the accuracy of lift and drag forces of the wings, the results were compared with wind tunnel experiments.

The flow domain constructed for the wings is cuboid and is based on an existing study in the literature [16]. The inlet section is located at a distance of about 5 times of the cord length from the leading edge to the front and the pressure outlet is 10 times the cord length from the leading edge towards the trailing edge of the wing. The lower and upper surfaces of the flow field were created at a distance of 5 times the length of the wing cord.

The length of the flow field was formed laterally 6 times the length of the wing cord and equal distance was released from the right and left sides. Structured and unstructured three-dimensional mesh models were implemented. To analyse the elaborative flow on the wing surface, five inflation layers were formed on the aerofoil with a growth rate of 1.2. The flow domain dimensions and mesh view are shown in Fig. 4. The analysis conditions were set to be the same as the wind tunnel experiments. The turbulence intensity is lower than %1, the Reynolds number is 2×10^5, the temperature is set to 300K and the pressure is 101,325pa. The wing surface is in the normal direction, the minimum grid spacing Δy^+ is between 0.3 and 0.7 at 0° angle for all wings. The mesh was performed according to the number of elements along the chord. For grid independence, the tests were modified in different element numbers in all wings at a zero angle, about 6×10^5, 1×10^6, 1.5×10^6, 2×10^6 and 2.5×10^6 respectively. Grid independence

Table 3. *The data of lift and drag force values obtained from studies according to mesh elements numbers (Since the table cannot fit on the page, "Study 1" values could not put into the table)*

|	Trial 2			Trial 3			Trial 4		
	Mesh Elements Numbers	**Lift Force (N)**	**Drag Force (N)**	**Mesh Elements Numbers**	**Lift Force (N)**	**Drag Force (N)**	**Mesh Elements Numbers**	**Lift Force (N)**	**Drag Force (N)**
b737a	1,073,838	0.1823	0.1480	1,550,530	0.1835	0.1495	2,074,452	0.1837	0.1498
b737b	986,767	0.1701	0.1223	1,453,724	0.1736	0.1261	2,080,300	0.1732	0.1271
b737c	1,144,929	0.1951	0.1116	1,546,707	0.1966	0.1143	2,019,227	0.1970	0.1152
b737d	1,050,723	0.1973	0.0914	15033141	0.2004	0.1020	2,016,543	0.2006	0.1031
Model Wing	941,582	0.1731	0.1081	1,564,569	0.1743	0.1222	2,182,051	0.1746	0.1237
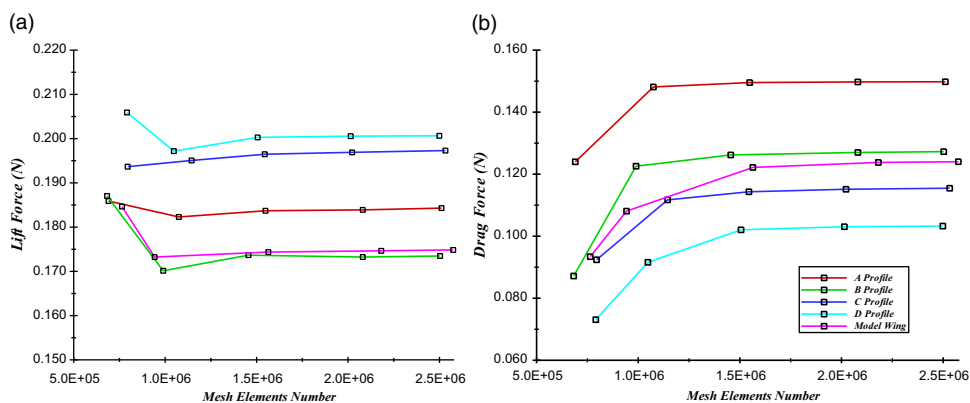
Figure 5. *The grid independency graphs (a) based on lift forces (b) based on drag forces.*

shows slight changes according to the model, but almost at all wings, as can be seen in Table 3, the grid independency obtained about 1.5×10^6. The grid independency based on lift and drag forces graphs are shown in Fig. 5. Since the results did not change after these numbers, which showed in Table 3, experiments were done to avoid time and energy loss.

3.2. Validation

This part summarises the common observations and discusses crucial features of wind tunnel test results and numerical analyses. In a series of angles of attack ranging from $-4°$ to the highest lift point (the max. angle varies depending on profile), a performance analysis of four different profiles and a rectangular wing formed from these profiles was performed at low Reynolds number Re $= 2 \times 10^5$.

Significant characteristics such as maximum lift, lift/drag coefficient (C_L/C_D), lift curve inclination and airflow behaviours were discussed. The results of numerical analyses have been validated with the data obtained from experimental tests for each profile and for the model wing. Figure 6 shows comparisons of lift coefficients (C_L) and lift/drag ratios (C_L/C_D) obtained from numerical studies and experimental tests versus angle-of-attack at Re $= 2 \times 10^5$ for some profiles and the model. As can be seen from the figures, for angles of attack between $4°$ and $16°$, the numerical results are almost the same as the experimental results. But for AoA $> 16°$, the differences in the lift coefficients become relatively large, and these differences can be explained by the complexity of the flow structure at a high angle-of-attack. In addition, although the numerical and experimental data are quite different from each
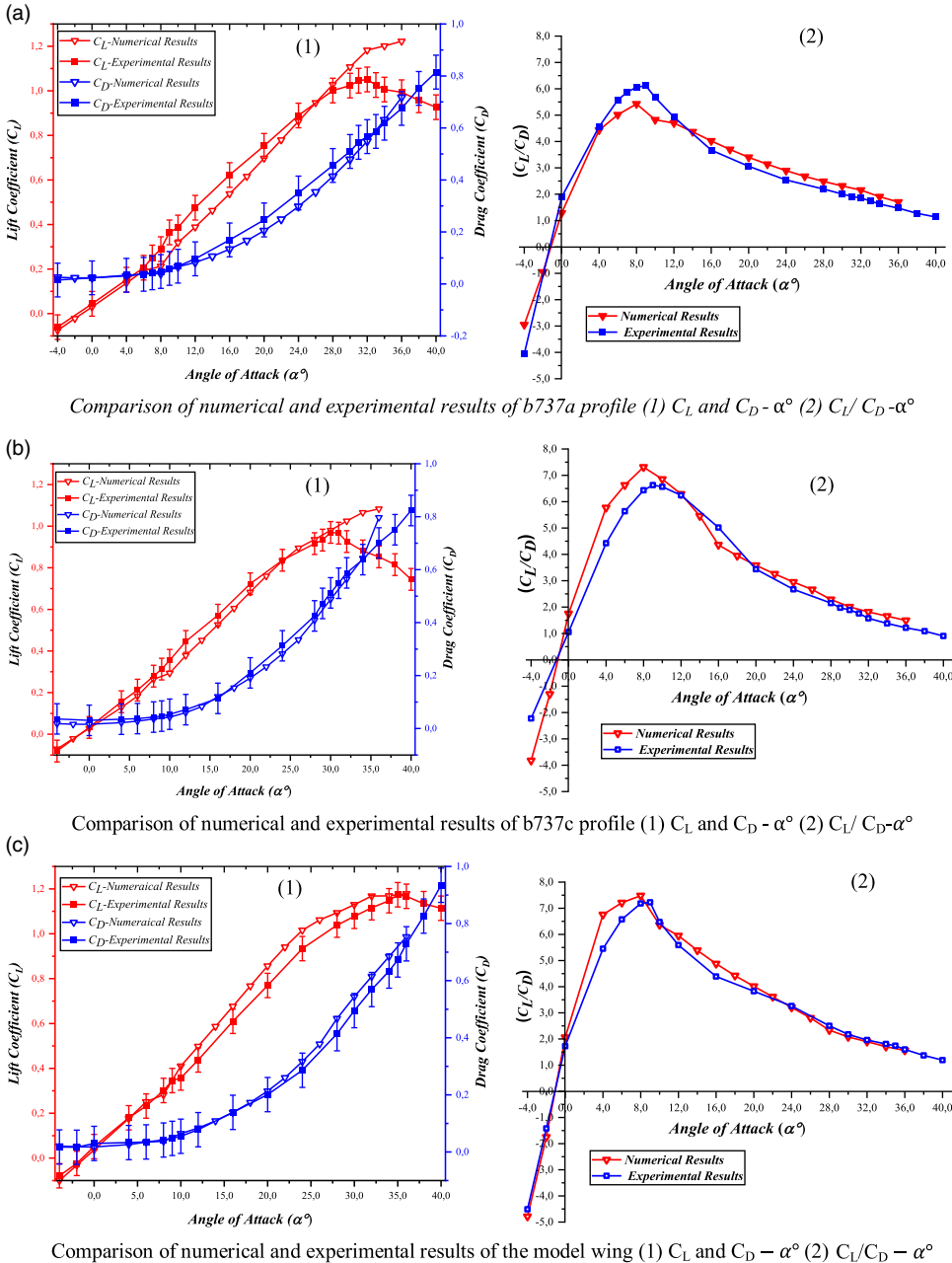
Comparison of numerical and experimental results of b737a profile (1) C_L and C_D - α° (2) C_L/C_D -α°

Comparison of numerical and experimental results of b737c profile (1) C_L and C_D - α° (2) C_L/C_D-α°

Comparison of numerical and experimental results of the model wing (1) C_L and C_D − α° (2) C_L/C_D − α°

Figure 6. *(a) Comparison of numerical and experimental results of b737a profile (1) C_L and C_D − α° (2) C_L/C_D −α°; (b) Comparison of numerical and experimental results of b737c profile (1) C_L and C_D − α° (2) C_L/C_D−α°; (c). Comparison of numerical and experimental results of the model wing (1) C_L and C_D − α° (2) C_L/C_D − α°.*

other at high angles of attack in the C_L charts, it is seen that there is consistency in these angles in the C_L/C_D charts. This is because drag forces at these angles gave quite different results from each other. In other words, drag force increased exponentially with the increase in lift force in numerical data, and this provided consistency in C_L/C_D graphics. As a result, the slopes of the numerical graphics are generally quite consistent with experimental results. The lift coefficients and C_L/C_D ratios values of numerical and experimental tests are shown in Table 4. Also, the angle values, which correspond to maximum

Table 4. C_L, C_D and C_L/C_D values of the profiles and the wing, the angle in which it is located and the drag coefficient that corresponds to this angle

	Numerical Results				**Experimental Results**			
	C_{Lmax}	**Located Angle ($\alpha°$)**	L/D_{max}	**Located Angle ($\alpha°$)**	C_{Lmax}	**Located Angle ($\alpha°$)**	L/D_{max}	**Located Angle ($\alpha°$)**
b737a-il	1.22	36°	5.42	8°	1.05	32°	6.11	9°
b737b-il	1.24	36°	6.1	8°	1.02	31°	6.1	9°
b737c-il	1.19	36°	7.31	8°	0.97	30°	6.56	10°
b737d-il	1.12	36°	6.48	8°	1.01	37°	6.16	8°
Model Wing	1.178	36°	7.48	8°	1.17	35°	7.22	9°

coefficient values, are given in the table. In this section, the values that determine the aerodynamic performances of the model wing and profiles are discussed.

As can be seen from Table 4, the highest lift coefficient has been obtained as 1.17 from the model wing at AoA = 35°, while among these highest lift coefficient points the lowest value has been tested as 0.97 from the 7c profile at AoA = 30°.

4.0 Results and discussions

4.1 Aerodynamic performance

The C_L/C_D ratio versus angle-of-attack and C_L versus C_D values obtained from experimental results graphs are given in Fig. 7. In Fig. 7(a), the changing lift coefficient of the profiles and the model wing versus the angle-of-attack is presented. As shown in the figure, the C_L values of the profiles and the wing have been measured close to each other at low and medium angles (between −4° and 14°). The highest C_L values have been obtained on the model wing at above AoA = 14°. The maximum coefficient is obtained as 1.05, 1.02, 0.97, 1.01 and 1.17 at 32, 31, 30, 37 and 35 degrees for profiles A, B, C, D and model wing, respectively.

In Fig. 7(b), the lift/drag ratio depending on the angle-of-attack has shown. The graph curves showed a similar trend to those in the literature, depending on the angle-of-attack [19, 20]. At the low angles, the graph curves show a very similar trend, while as the angle-of-attack increases the clearance between curves have risen too. In particular, the gap between the curves at an angle of 8°, at which maximum lift/drag ratios are obtained, has reached its maximum value. Such different performance exhibits of the wings are due to characteristic features such as the thickness and the cambre of the profiles.

As shown in Fig. 7(b), profile A which has a higher thickness, has shown lower performance than other profiles and model wings at lower angles because of the high drag force obtained from the profile. The other profiles have followed closer performance to each other, but as the thickness of the profiles decreased, the wings have seen to perform better performance. Above AoA = 28°, the model wing has shown the same results considering C_L/C_D. In addition, it seems to be another remarkable situation that the model wing generally produces the highest C_L/C_D ratio. As shown in Fig. 7(b) and Table 4, the highest C_L/C_D ratio has been measured as 7.22 from the model wing at AoA = 9°.

Moreover, the highest values for all profiles and for the model wing have been obtained at AoA = 7°–9°. Above these angles, it can be seen that the C_L/C_D ratios are decreasing with the increasing of angle for all profiles and the model wing. At the AoA = 7°–9°, among these, the highest C_L/C_D ratio points to the lowest ratio have been measured as 6.1 from 7a and 7b profiles.

In Fig. 7(c), the change of the lift coefficient with the drag coefficient (C_D) is shown. The curves have shown a very close performance to each other in general at lower angles. It is seen that the curve of the model wing generally exhibits better performance for a constant drag coefficient because of having a higher lift and a lower drag, compared to the others.
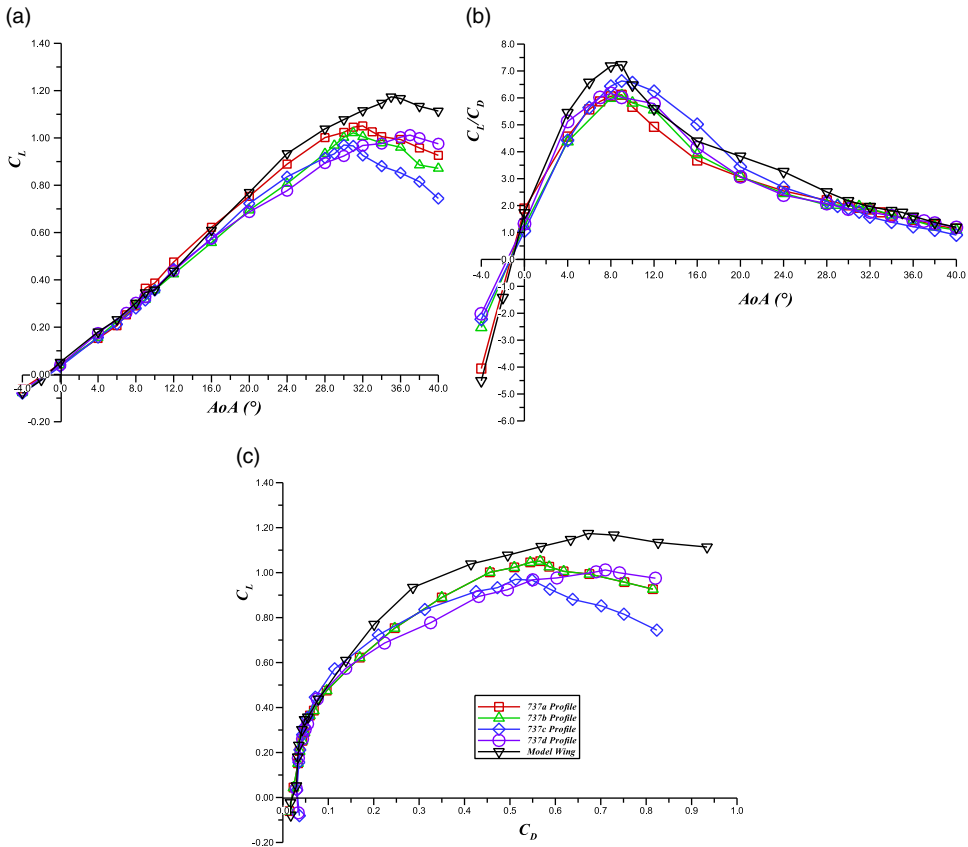
Figure 7. *Graphs of the profiles and the model wing (a) C_L coefficients; (b) C_L/C_D ratios versus angle-of-attack; (c) C_L versus C_D.*

4.2. Pressure distribution

The pressure coefficients (C_P) distributions of given with equation (3) versus x/c for different AoA and different profiles at different positions on profiles ($z/b = 5\%$, 25%, 50%) are shown in Figs. 8, 9, 10 and 11 and on model wing ($z/b = 5\%$, 33.3%, 66.6% and 95%) is shown in Fig. 12. In all graphs, x/c is in the range of "0 to 1.0" in the X-direction, and z/b is in the range of "-6.5 to 2" in Y-direction. It is observed that at $8°$ angle-of-attack for all C_P data, lower and upper surface curves are very close to each other. It is seen that increasing with the angle-of-attack ($20°$) the pressure coefficient on the upper surface of the leading edge side of the wing reaches the peak quickly and then decreases smoothly while the curves on the lower surface increase thus the shear between the two curves is opened. As found in literature study, this is typical behaviour of the static pressure on the wing [9, 21, 22, 23]. There is generally no large oscillation at a relatively small angle ($8°$), while at $32°$ angle-of-attack, especially due to tip vortices at the wing-tip planes, some oscillations are seen to take place.

According to Fig. 6, it is understood that no flow separation occurs at the wing surface at the angle-of-attack of $0°$ and $8°$ angle-of-attack. But at $16°$ a slight separation occurred on the wing surface at the leading-edge side, and this separation covered about 20% of the wing cord on $z/b = 25\%$ and $z/b = 50\%$. After this point, the flow is re-attached to the wing surface. But at $z/b = 5\%$, the flow is separated from the surface along the cord and a separation bubble has occurred due to the tip vortexes. Laminar separation bubbles have not formed along the cord on the wing surface at $z/b = 5\%$ and 25% for $8°$ and $20°$. For 50% of the cord, it is seen to form and re-attach laminar separation bubbles at the angles. At the $30°$
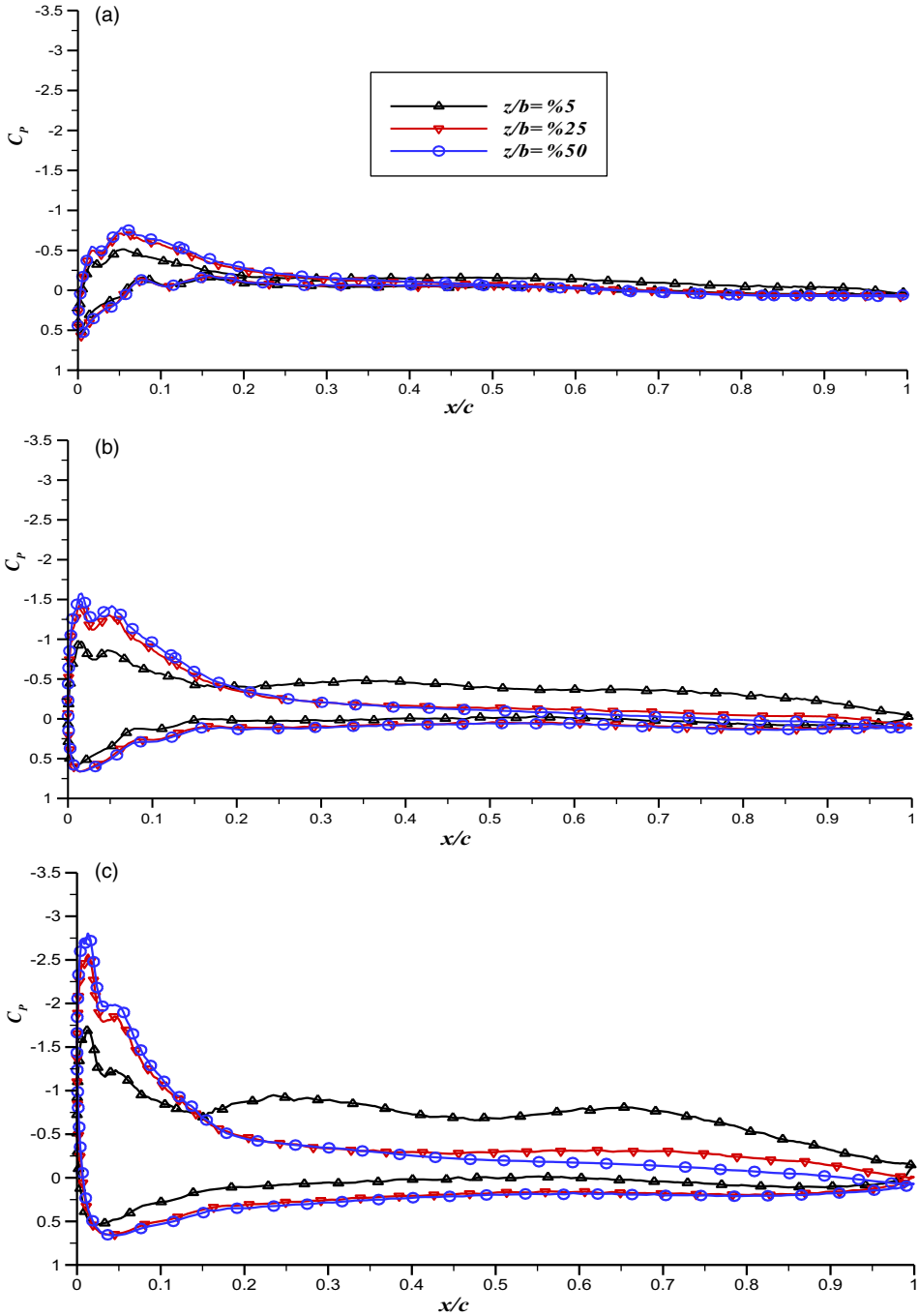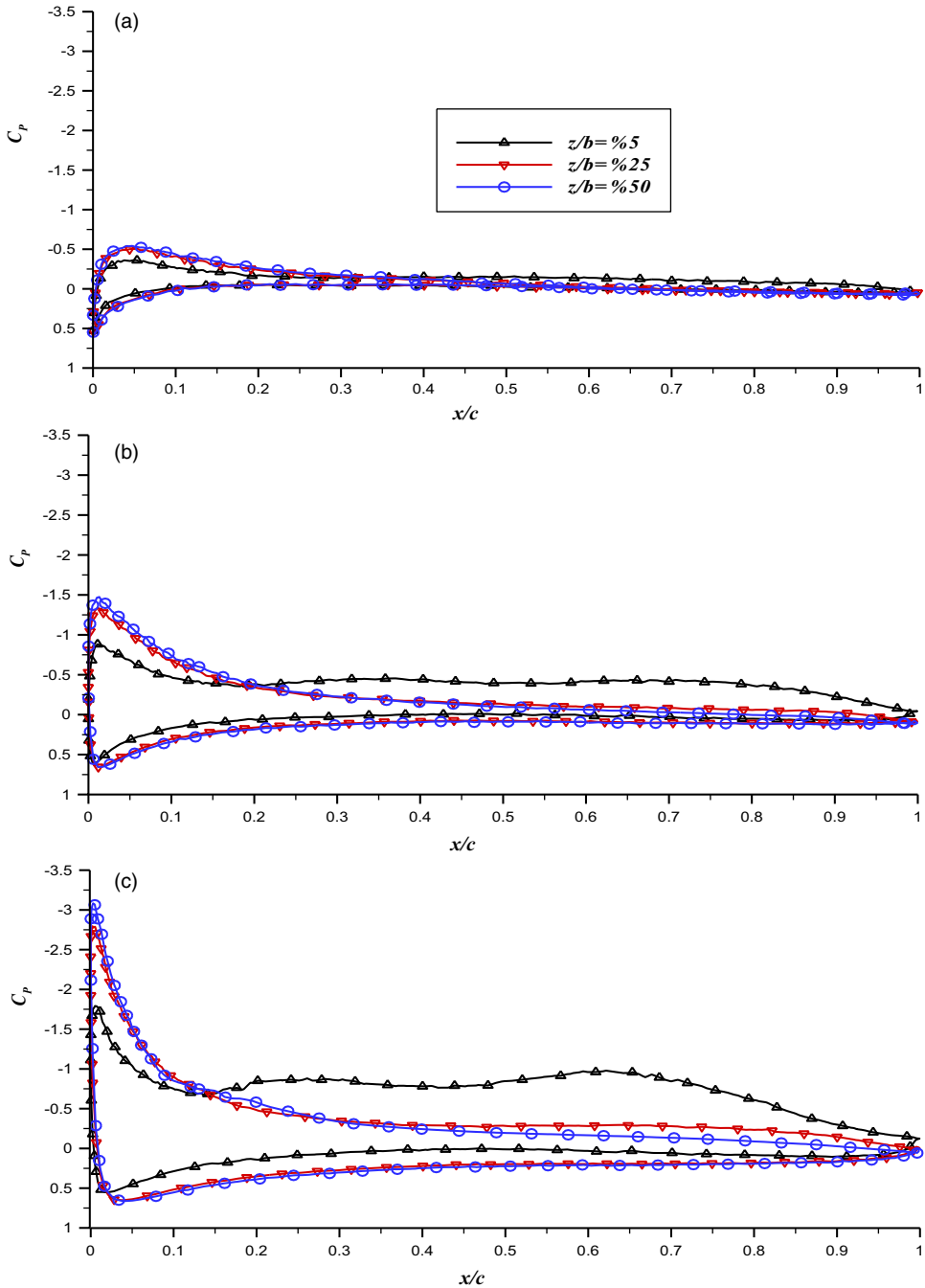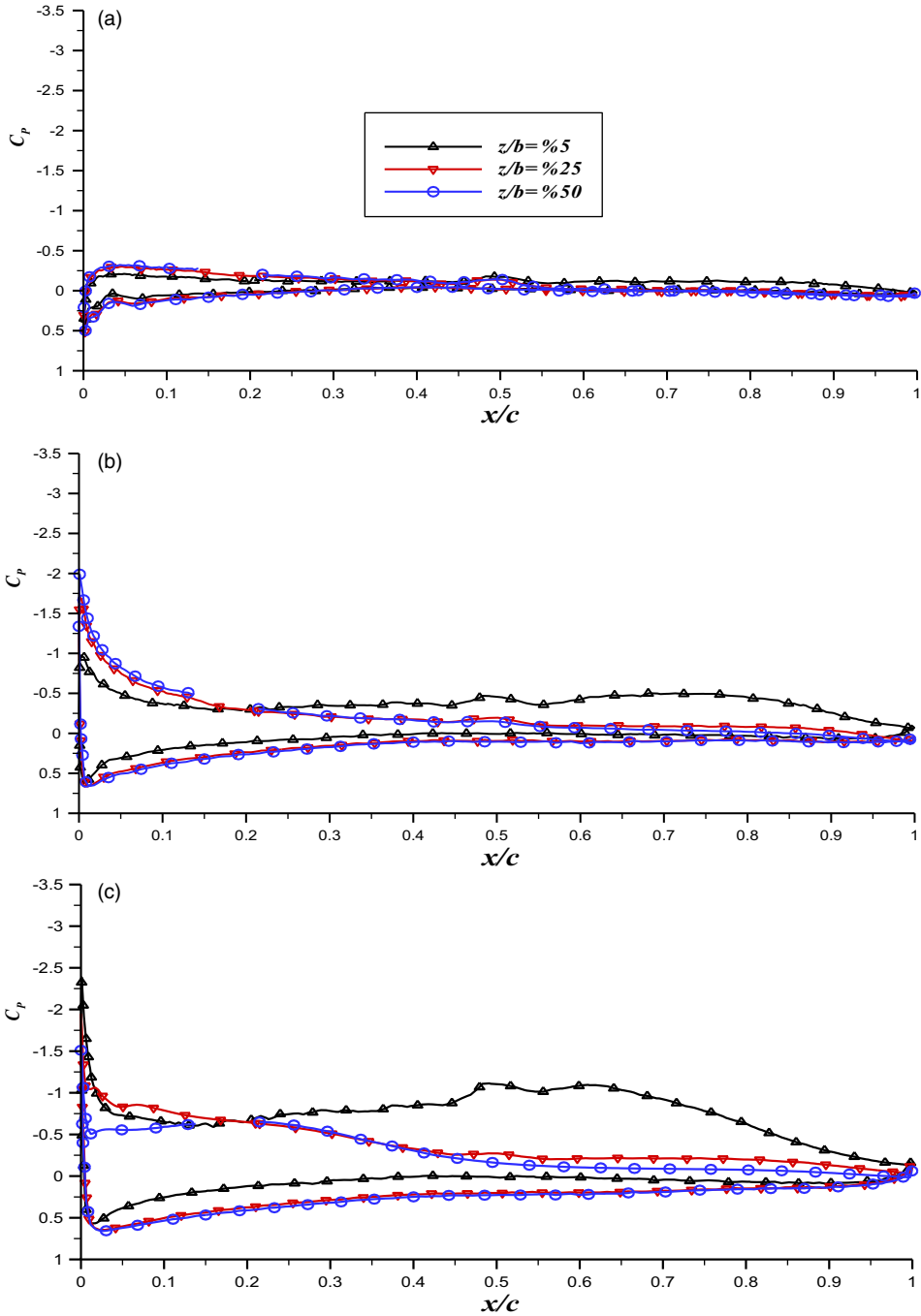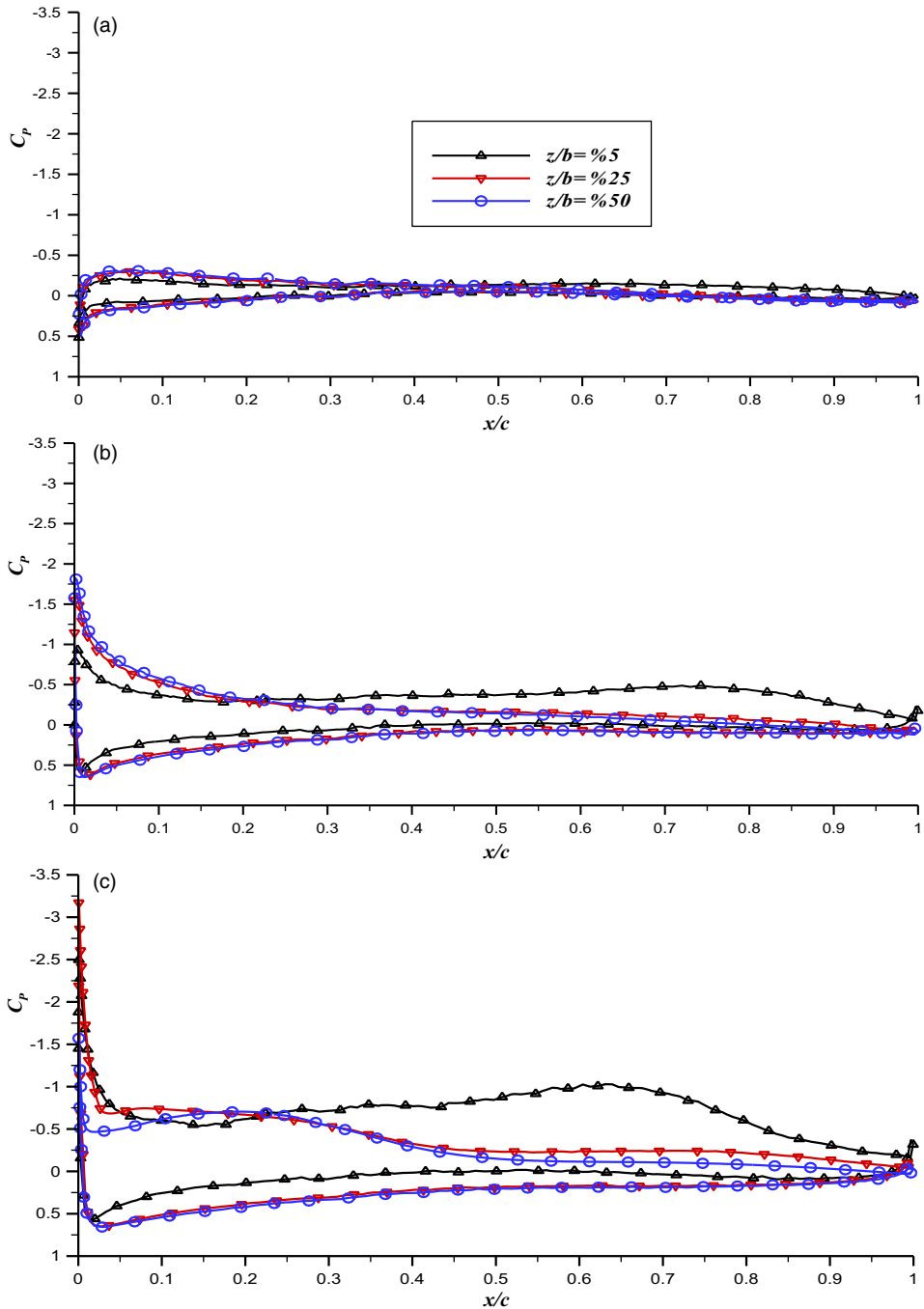
Figure 8. *The distributions of pressure coefficients (C_P) of profile A (b737a-il) versus x/c for different plane (z/b = 5%, 25% and 50%) and different AoA (a) α =8° (b) α =20° (c) α =32°.*

Figure 9. *The distributions of pressure coefficients (C_P) of profile B (b737b-il) versus x/c for different plane (z/b = 5%, 25% and 50%) and different AoA (a) α = 8° (b) α = 20° (c) α = 32°.*

Figure 10. *The distributions of pressure coefficients (C_P) of profile C (b737c-il) versus x/c for different plane (z/b = 5%, 25% and 50%) and different AoA (a) α = 8° (b) α = 20° (c) α = 32°.*

Figure 11. *The distributions of pressure coefficients (C_P) of profile D (b737d-il) versus x/c for different plane (z/b = 5%, 25% and 50%) and different AoA (a) α = 8° (b) α = 20° (c) α = 32°.*
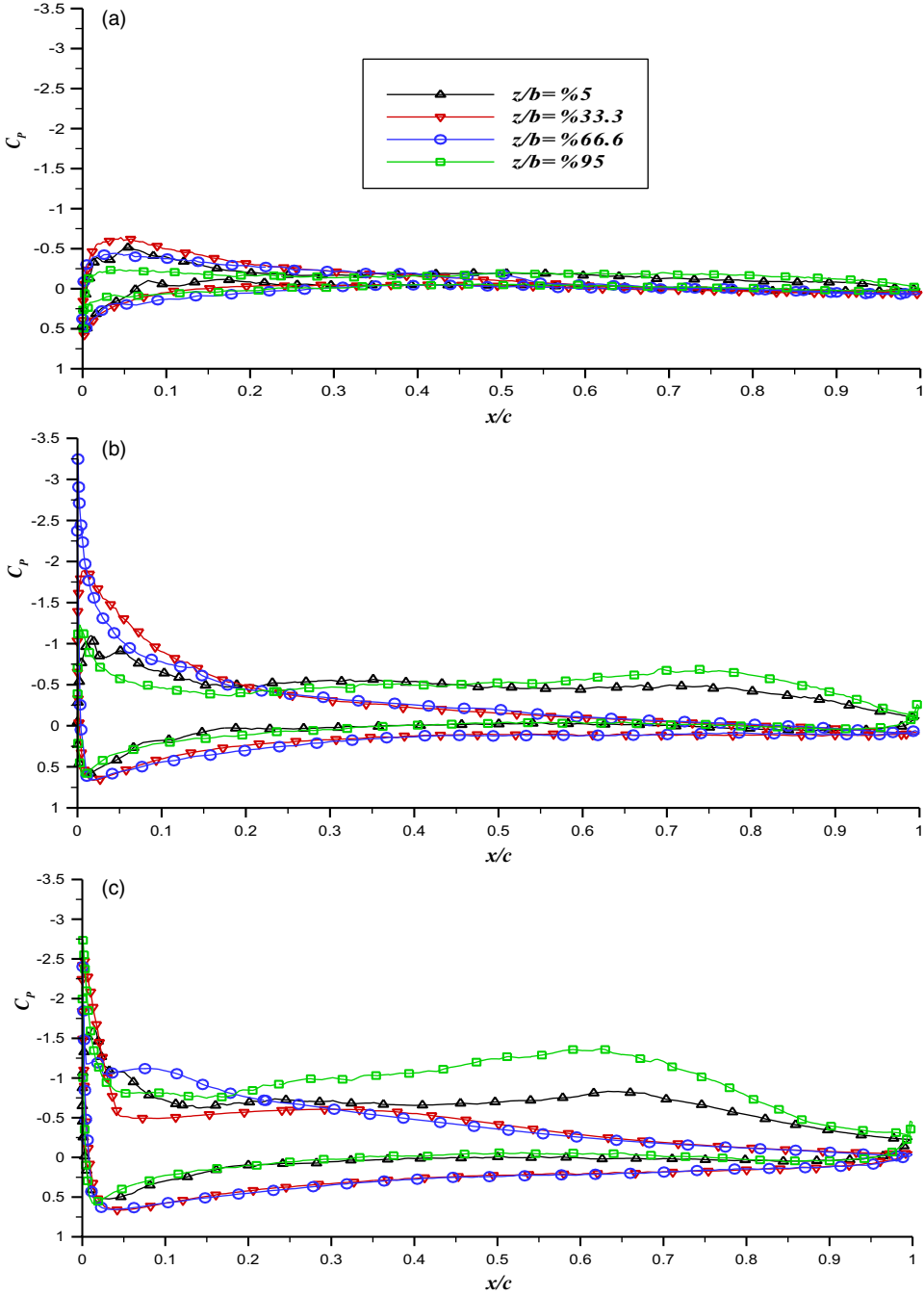
Figure 12. *The distributions of pressure coefficients (C$_P$) of model wing versus x/c for different plane (z/b = 5%, 33%, 66% and 95%) and different AoA (a) α = 8° (b) α = 20° (c) α = 32°.*
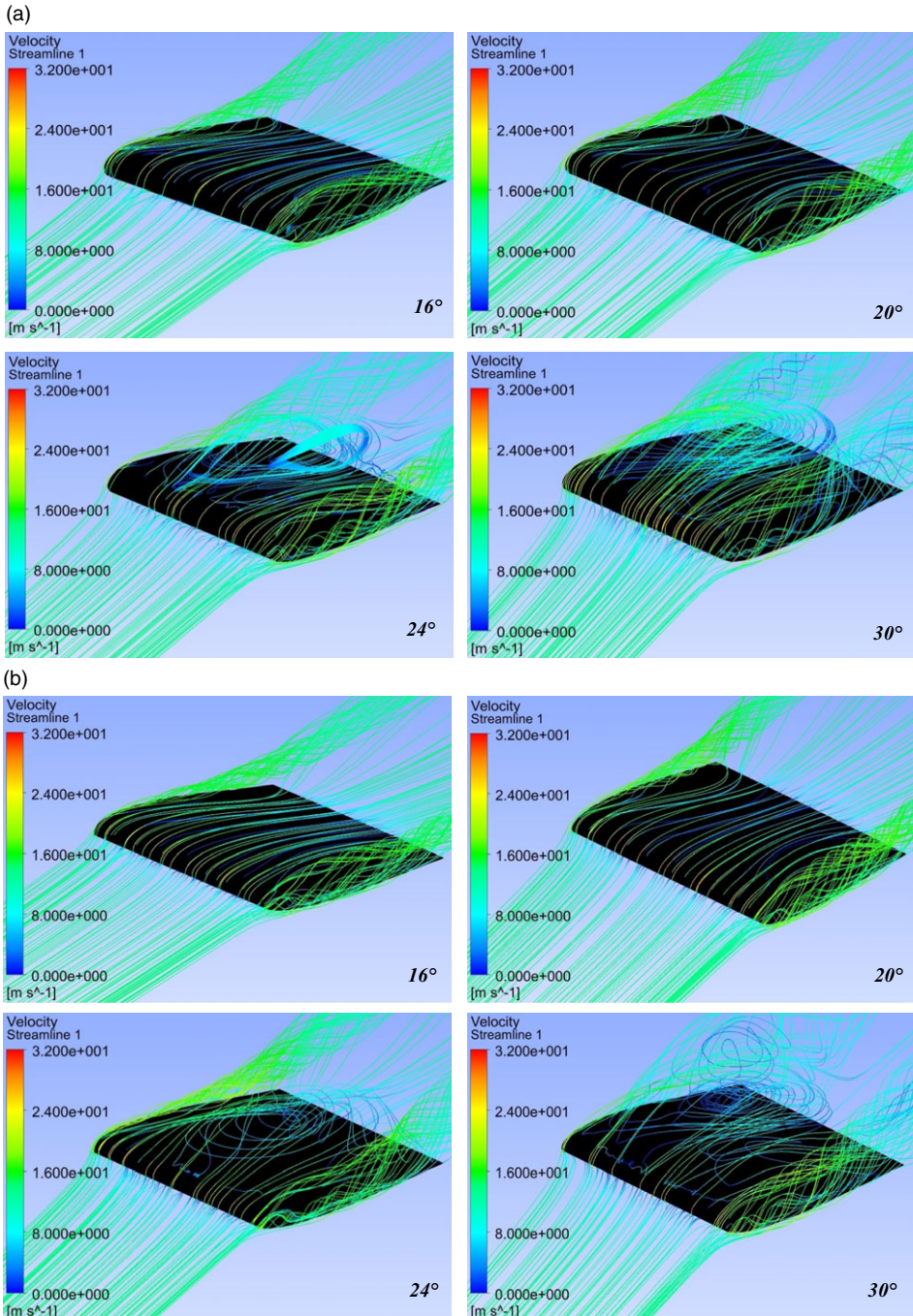
(a)

(b)

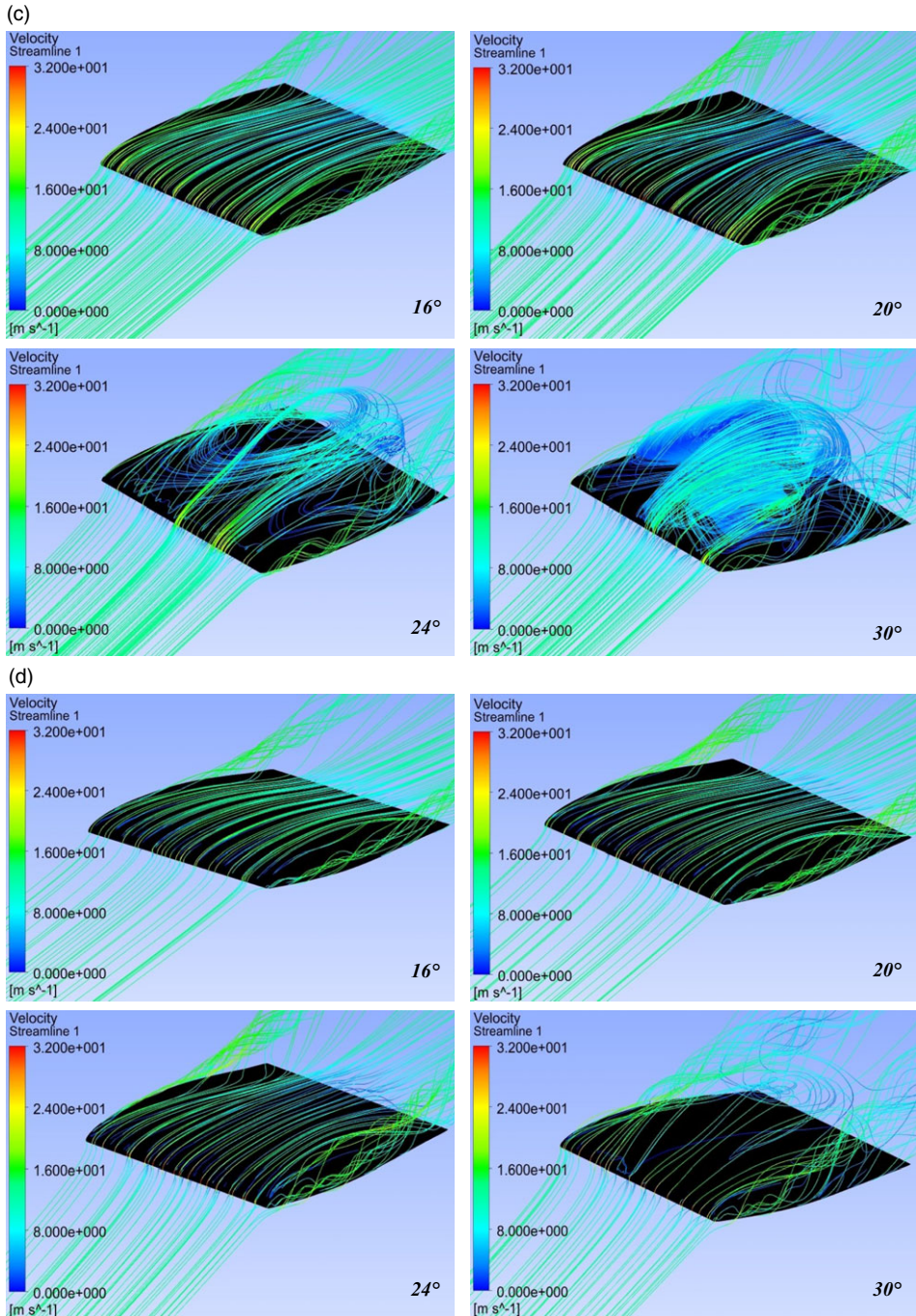
Figure 13. *Continued.*

(c)

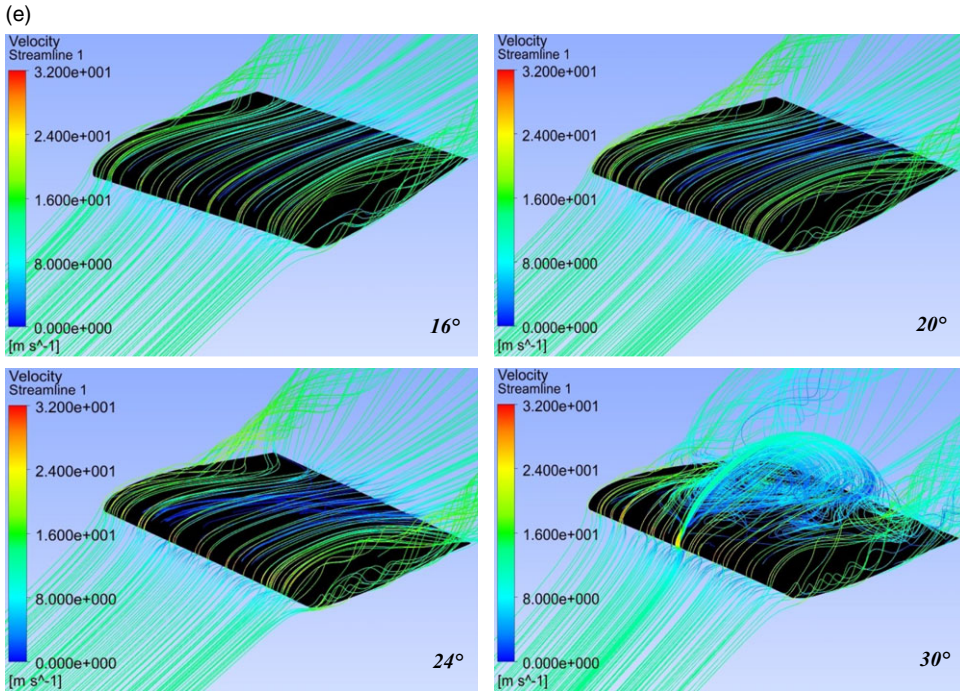

(d)

Figure 13. *Continued.*

Figure 13. *The changes of velocity with streamline around the profiles and the model wing (a) 737a-il profile; (b) 737b-il profile; (c) 737c-il profile; (d) 737d-il profile; (e) model wing.*

angle-of-attack, the laminar separation bubbles were formed along the cord in all planes and the wings were found to stall exactly.

When the pressure distributions on the planes are compared, while the $z/b = 25\%$ and $z/b = 50\%$ show almost the same distribution, the $z/b = 5\%$ shows a different distribution from the other two because of tip vortexes. All of the above interpretations also apply to the pressure distributions of the model wing given in Fig. 12. In the tip-planes the laminar separation bubbles have occurred along the cord, while in the mid-section of the wing the flow has reattached to the wing surface after about 50% of the cord.

In summary, it is seen that laminar separation bubbles form due to the wing tip vortex in the regions close to the wing tip ($z/b = 5\%$ or 95%). Furthermore, it is said that these separations have spread over the entire surface at a high attack angle (AoA $= 30°$).

$$C_p = \left[\frac{(P - P_\infty)}{\frac{1}{2} * \rho_\infty * U_\infty^2} \right] \tag{3}$$

In equation (3), the P is the static pressure at the point that the pressure coefficient is evaluated; P_∞ is the static pressure in the free-flow; ρ_∞ is the free flow density, and U_∞ is the freestream velocity of the fluid.

4.3. Velocity streamlines and smoke flow visualization

The velocity streamlines around the profiles are given in Fig. 13. In addition, pictures of smoke flow visualisation for different angles of attack are shown in Fig. 14. It is seen that the air flows smoothly on all of the wing surfaces at AoA $= 20°$ and below.

Besides this, as can be seen in stream lines, the flow is separated from the leading-edge side of the wing surface slightly for a very short distance but then re-attached to the surface at AoA $= 16°$ and 20°.
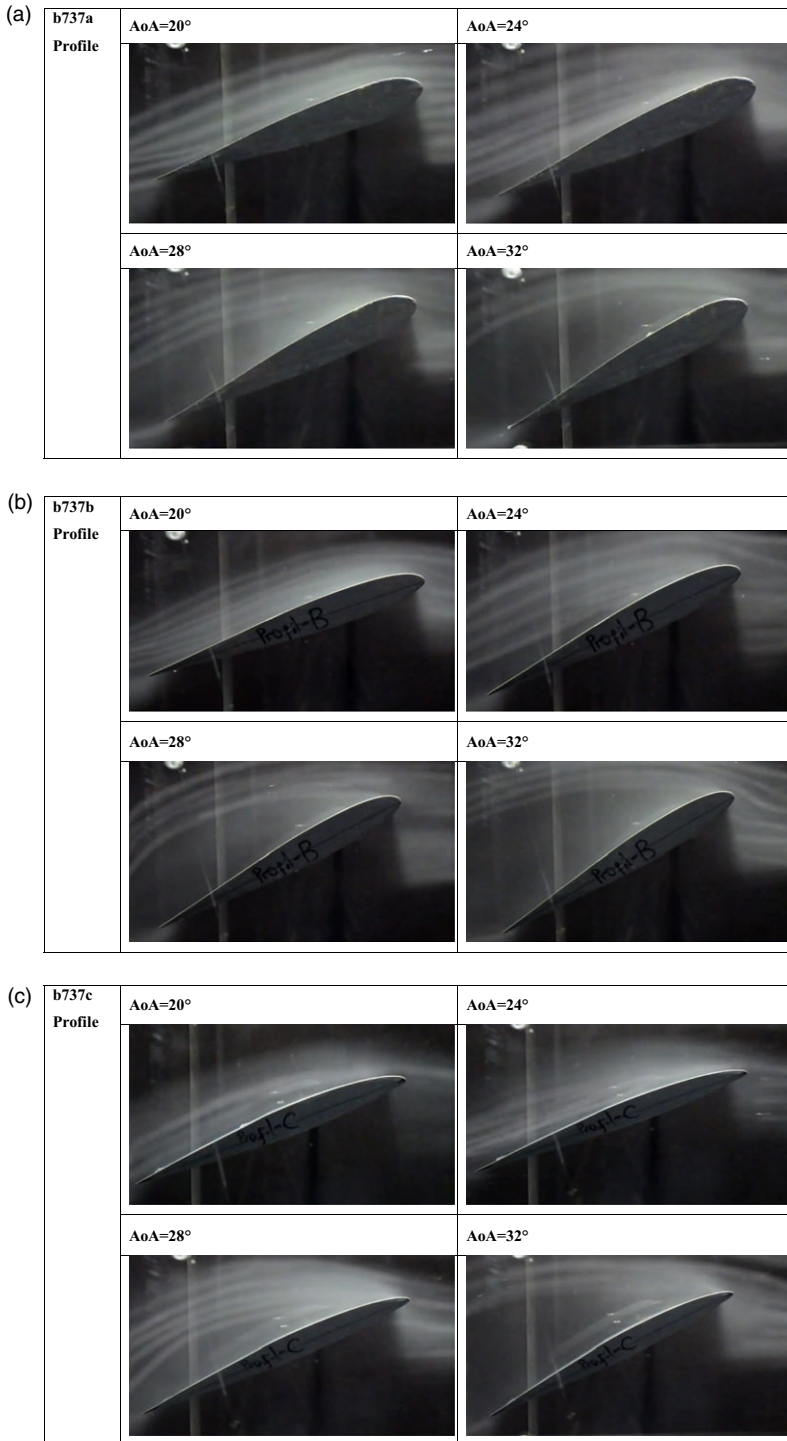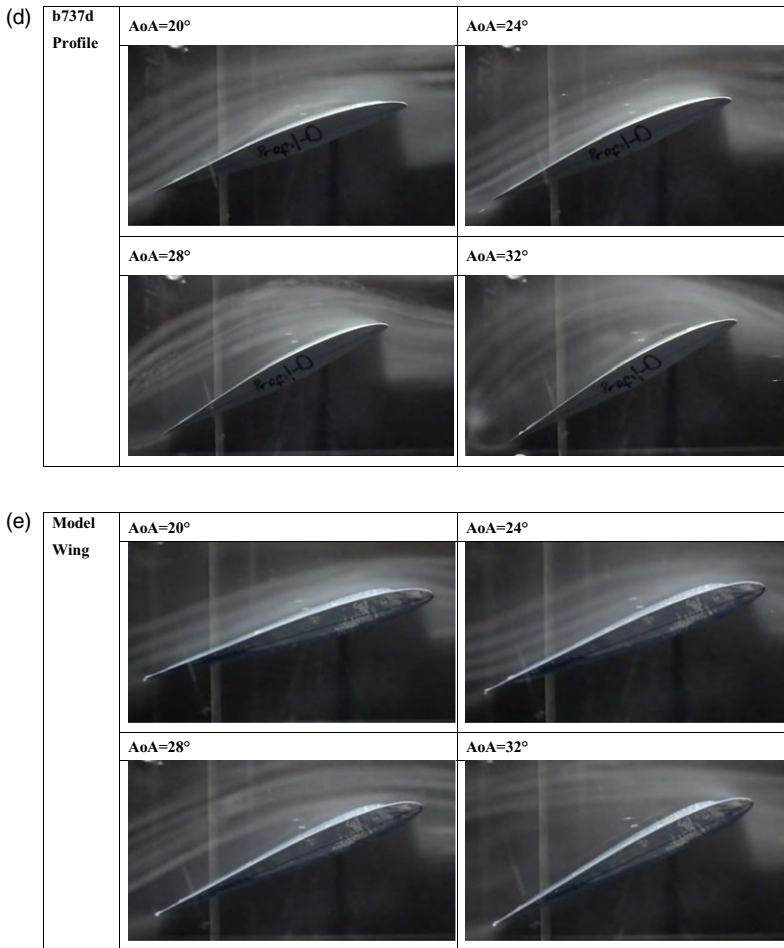
Figure 14. Continued.

Figure 14. *(a) Pictures of smoke flow visualisation for different angles of attack on b737a profile; (b) Pictures of smoke flow visualisation for different angles of attack on b737b profile; (c) Pictures of smoke flow visualisation for different angles of attack on b737c profile; (d) Pictures of smoke flow visualisation for different angles of attack on b737d profile; (e) Pictures of smoke flow visualisation for different angles of attack on model wing.*

At the 20° angle-of-attack, as expected, it seems that the flow started to separate from the trailing edge of the wing (especially profiles A and B) and as the angle-of-attack increased (AoA = 24°), the separation point approached the middle of the upper surface. In this sense, similar results were obtained from the studies in the literature [24].

For the 24° in streamline pictures, laminar separation bubble has taken place on the 7a, 7b and 7c profiles while on the 7d profile only a flow separation has formed at the trailing edge of the wing and the laminar separation bubble has not yet formed. Also, the laminar separation bubble has not formed yet over the model wing too, only flow separation occurred on the middle part of the wing. When the smoke pictures are investigated, the laminar separation bubbles have seen to begin at 28°. In addition, it can be seen clearly that the laminar separation bubble over the model wing surface is very small than the bubbles over the profiles.

Over 24°, the flow separation point moves towards the leading edge with an increasing angle-of-attack. At the 30° and 32° the laminar separation bubble has occurred over all of the profiles and model

wing. It can also be seen that the poured vortexes from the wing tips are moving towards the middle section of the wings.

Flow separation and separation bubbles usually appear to occur in the middle of the wings. Similar to studies in the literature [25], it can be said that vortexes on the edges of the wings have an inhibiting effect on the complete separation of the flow. But at the same time, it causes both the lift force decrease and the drag force to increase. As the angle-of-attack increases the wing-edge vortexes are seen to spread towards the mid-section of the wing, also raised in both height and density.

5.0 Conclusions

In this study, four different profiles used in Boeing 737-Classic aircraft wings and a model wing which is a combination of these profiles were investigated between $-4°$ to the maximum lift point and at the 2×10^5 Reynolds number and the results were compared. The results were validated by comparing the numerical and experimental data. It was observed that as the thickness of the profiles decreased, the wing performance increased in terms of lift/drag ratio at the angles where the C_L/C_D ratio is max. In addition, the best performance has been observed with the model wing. At low angles of attack, the flow on the wings was laminar, and as the angle-of-attack increased, flow separation from the trailing edges on the wings occurred and as the angle increased, the separation point approached the leading edge. Despite the formation of a separation bubble on the profiles at 24° angle, the model wing has not yet formed. At a 30° attack angle, separation bubbles were formed in all the profiles and on the middle part of the model wing. The growth of the separation bubbles has created an extra carrying force, but at the same time caused a larger drag force too. As a result, it has caused decreasing in the lift/drag ratio. Owing to the separation bubbles, as seen in the Cp graphs, fluctuations have taken place in the pressure distribution over the upper surface of the wing. As can be seen from the Cp graphs, the wing vortexes caused a separation at the ends of the attack angle of 24° and above.

Data availability statement. All data used during the study are available from the corresponding author by request.

References

[1] Lissaman, P.B.S. Low-reynolds-number airfoils, *Ann. Rev. Fluid Mech.*, 1983, **15**, pp 223–239.

[2] Crompton, M.J. and Barrett, R.V. Investigation of the separation bubble formed behind the sharp leading edge of a flat plate at incidence, *Proc. Inst. Mech. Eng. G J. Aerosp. Eng.*, 2000, **214**, pp 157–176.

[3] McCullough, G.B. and Gault, D.E., Examples of three representative types of airfoil-section stall at low speed, *NACA TN*, 1951, **2502**, pp 1–53.

[4] Roberts, W.B. Calculation of laminar separation bubbles and their effect on airfoil performance, *AIAA J.*, 1980, **18**, pp 25–31.

[5] Lei, J., Guo, F. and Huang, C. Numerical study of separation on the trailing edge of a symmetrical airfoil at a low Reynolds number, *Chinese J. Aeronaut.*, 2013, **26**, 918–925.

[6] Spalart, P.R. and Strelets, M.K., Mechanisms of transition and heat transfer in a separation bubble, *J. Fluid Mech.*, 2000, **403**, pp 329–349.

[7] Houghton, D.T., Carpenter, E.L., Collicott, P.W. and Valentine, S.H. *Aerodynamics for Engineering Students*, Sixth Edition, Elsevier Ltd, United States, 2013.

[8] Simpson, R.L. Turbulent boundary-layer separation, *Ann. Rev. Fluid Mec.*, 1989, **21**, pp 205–234.

[9] Yang, Z., Haan, F.L., Hui, H. and Ma, H., An experimental investigation on the flow separation on a low-reynolds-number airfoil, In *45th AIAA Aerosp. Sci. Meet. Exhib,* pp 1–11, 2007.

[10] Zanin, B.Y., Kozlov, V.V. and Pavlenko, A.M. Control of flow separation from a model wing at low Reynolds numbers, *Fluid Dyn.*, 2012, **47**, pp 403–410.

[11] Mack, S., Brehm, C., Heine, B., Kurz, A. and Fasel, H.F., Experimental investigation of separation and separation control on a laminar airfoil, In *4th AIAA Flow Control Conference*, June. Seattle, WA, United States, 2008.

[12] Karasu, İ., Genç, M.S., Açıkel, H.A. and Akpolat, M.T., An experimental study on laminar separation bubble and transition over an aerofoil at low reynolds number, In *30th AIAA Applied Aerodynamics Conference, Fluid Dynamics and Co-located Conferences*, vol. 3, pp 1–9, 2012.

[13] Aşkan, A. and Tangöz, S. The impact of aspect ratio on aerodynamic performance and flow separation behavior of a model wing composed from different profiles, *J. Energy Syst.*, 2018, **2**, (4), pp 224–237.

[14] Yilmaz, İ., Çam, Ö., Taştan, M. and Karci, A. Experimental investigation of aerodynamic performance of different wind turbine airfoils, *Politeknik*, 2016, **9**, pp 577–584.

[15] Coleman, H.W. and Steele, G. *Experimentation and Uncertainty Analysis for Engineers*, 4th edition, Wiley, New York, 2018.

[16] Chen, P., Bai, C. and Wang, W. Experimental and numerical studies of low aspect ratio wing at critical Reynolds number, *Eur. J. Mech. B/Fluids*, 2016, **59**, pp 161–168.

[17] Langtry, R. and Menter, F. Transition modeling for general CFD applications in aeronautics, In *43rd AIAA Aerosp. Sci. Meet. Exhib.*, pp 1–14, 2005.

[18] Şugar Gabor, O., Koreanschi, A., Botez, R.M., Mamou, M. and Mebarki, Y. Numerical simulation and wind tunnel tests investigation and validation of a morphing wing-tip demonstrator aerodynamic performance, *Aerosp. Sci. Technol.*, 2016, **53**, pp 136–153.

[19] Shields, M.C. and Mohseni, K. Aerodynamic stability modes of low aspect ratio wings, In *AIAA Guid. Navig. Control Conf.*, pp 1–15, 2013.

[20] Zhang, Z., Hubner, J.P., Timpe, A., Ukeiley, L., Abudaram, Y. and Ifju, P. Effect of aspect ratio on flat – plate membrane airfoils, In *50th AIAA Aerosp. Sci. Meet. Incl. New Horizons Forum Aerosp. Expo.*, January, pp 1–15, 2012.

[21] Hu, H. and Yang, Z. An experimental study of the laminar flow separation on a low-reynolds-number airfoil, *J. Fluids Eng.*, 2008, **130**, pp 1–11.

[22] Worasinchai, S., Ingram, G. and Dominy, R. A low-Reynolds-number high-angle-of-attack investigation of wind turbine aerofoils, *Proc. Inst. Mech. Eng. A: J. Power Energy*, 2011, 225, pp 748–763.

[23] Zhang, W., Zhang, Z., Chen, Z. and Tang, Q. Main characteristics of suction control of flow separation of an airfoil at low Reynolds numbers, *Eur. J. Mech. B/Fluids*, 2017, **65**, pp 88–97.

[24] Khakmardani, M.H., Soltani, M.R., Masdari, M. and Davari, A. An experimental investigation of transition point over a quasi-2D swept wing by using hot film, *Proc. IMechE G: J. Aerosp. Eng.*, 2015, **229**, (2), pp 243–255.

[25] Soylak, M., Experimental investigation of aerodynamic performance of oscillating wings at low Re numbers, *Proc. IMechE G: J. Aerosp. Eng.*, 2015, **230**, (10), pp 1882–1902.